



Characterization of a macro porous polymer membrane at micron-scale by Confocal-Laser-Scanning Microscopy and 3D image analysis



Adrian Ley^{a,b}, Patrick Altschuh^d, Volkmar Thom^b, Michael Selzer^{c,d}, Britta Nestler^{c,d}, Philipp Vana^a

^a Institute for Physical Chemistry, Georg-August-University Goettingen, Tammannstraße 4, 37077 Goettingen, Germany

^b Sartorius Stedim Biotech GmbH, August-Spindler-Strasse 11, 37079 Goettingen, Germany

^c Institute of Digital Material Science, Karlsruhe University of Applied Sciences, Moltkestrasse 30, 76133 Karlsruhe, Germany

^d Institute for Applied Materials, Karlsruhe Institute of Technology (KIT), Strasse am Forum 7, 76131 Karlsruhe, Germany

ARTICLE INFO

Keywords:

CLSM
3D image analysis
Porous polymer membrane
Diagnostic membrane
Membrane characterization

ABSTRACT

Due to the structural complexity of phase inversion macroporous polymer membranes there is a general need for characterization methods on the pore size scale of such membranes. Structure characteristics like pore size distribution, porosity, pore size gradient and the specific surface area often have an impact on the requested performance of such membranes in their field of usage. Here, a commercially available, symmetric, phase inversion nitrocellulose membrane, typically applied in lateral flow immunoassays in the field of in-vitro diagnostics, is investigated. However, commonly used methods for the determination of these characteristics are either cumulative methods, not being able to resolve a 3D pore structure on a local level, or are limited in their ability to reproducibly quantify pore size characteristics. The proposed membrane characterization method uses confocal laser scanning microscopy (CLSM) images combined with computer based image analysis to derive a complete 3D representation of the membrane structure with sufficient resolution and a quantitative characterization thereof. In order to extract quantifiable structural information, the CLSM derived images are binarized using a suitable threshold to match experimental values for porosity. Afterwards a signed distance function is calculated in the 3D structure measuring the smallest distances between pore boundaries followed by a medial axis marking the center of the signed distance function. Structure characteristics like pore size distribution, porosity and specific surface area of the membrane can be determined on a local level. Furthermore, using Stokes equation, the permeability of the membrane is calculated to support the 3D representation obtained by CLSM and the structure characteristics determined by computer based image analysis. Pore size distribution and permeability derived by image analysis show very good agreement with experimental values for the membrane.

1. Introduction

Commonly used methods for the pore structure characterization of macro porous membranes, like e.g. permeability, capillary flow porometry [1–4], BET-analysis [5] or Bubble Point measurements [6,7] produce integral structure parameters that do not give locally resolved information. Although this information is quite important as it often correlates with the performance of the membrane, local structure information, especially along the thickness of the membrane, can be very helpful for the full consideration of this performance. Scanning electron microscopy (SEM) and CLSM image analysis of differently prepared membrane samples have been used to generate locally resolved structural information [8–10], however, due to the 2D character of SEM

imaging techniques and the reported 2D CLSM images, where only a single optical section was recorded, a quantitative evaluation of pore structure is not possible. Based on different methods of 3D structure imaging and image analysis, alternative techniques have been developed, like x-ray diffraction [10], imaging of resin filled membranes [11–13], or CLSM, by recording a series of single optical sections, as proposed by Charcosset et.al. [14,15]. All these techniques are limited in their ability to extract quantitative structural information from the images. Sample preparation usually requires artificial conditioning far from the application. The aim of this work is to generate a sufficiently resolved 3D representation of commercial lateral flow membranes [16,17] under application relevant conditions in order to extract quantitative structural information and to enable enhanced structure-

E-mail addresses: adrian.ley@sartorius.com (A. Ley), patrick.altshuh@kit.edu (P. Altschuh), volkmar.thom@sartorius.com (V. Thom), michael.selzer@hs-karlsruhe.de (M. Selzer), britta.nestler@kit.edu (B. Nestler), p.vana@gwdg.de (P. Vana).

<https://doi.org/10.1016/j.memsci.2018.07.062>

Received 11 May 2018; Received in revised form 17 July 2018; Accepted 24 July 2018

Available online 26 July 2018

0376-7388/ © 2018 Elsevier B.V. All rights reserved.

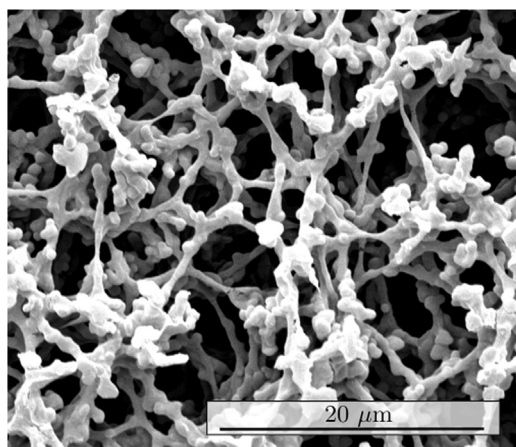


Fig. 1. Scanning electron microscopy image (SEM) of the analyzed porous membrane microstructure with a magnification of 8000 \times . The image was taken by a (FEI) Quanta 200F.

performance correlations. CLSM combined with computer-assisted image evaluation was employed to generate 3D representations of a fluorescently labeled macroporous nitrocellulose membrane. Using an algorithm that is based on a signed distance function and the generated medial axis for each pore, spheres can be fitted into the porous 3D structure. Using the size distribution of these spheres, the pore size distribution of the membrane can be determined on a local level. In order to validate the 3D representation obtained by CLSM, the structural characteristics obtained by computer-based image analysis i.e. specific surface area, pore size distribution, permeability of the membrane, are compared to experimental values. In this study, a commercial available phase inversion, macroporous nitrocellulose membrane is investigated. This membrane is commonly used in lateral flow immunoassays like e.g. the home pregnancy test. Due to their simple layout, lateral flow immunoassays are also used in the field of infectious diseases, drugs of abuse and oncology where the macroporous phase inversion nitrocellulose membrane is responsible for a capillary driven transport of a sample fluid. Since nitrocellulose membranes exhibit relatively high binding capacity for proteins without affecting the activity of the bound protein, antibodies can be printed onto the membrane [16,17]. The phase inversion derived membrane exhibits a highly porous and complex microstructure (see Fig. 1).

2. Materials and methods

All experiments were performed on Unisart©140, a commercially available, unsupported, nitrocellulose membrane for lateral flow immunoassay membrane (Sartorius Stedim Biotech GmbH) with a nominal pore size of 8 μm , a thickness of 142 μm , and a wicking speed of ~ 120 s/40 mm. In order to reduce variations due to structural inhomogeneities, all measurements were performed on the same membrane samples. First, eight circular samples with a diameter of 47 mm were used to determine the porosity and water permeability 2.3.4. The samples were then subject to a BET analysis. Afterwards 25 mm diameter cut outs were taken from the center of each of the 47 mm diameter samples for capillary flow porometry. Eventually, sixteen cut-outs with 10 mm diameter were taken from the 25 mm samples to carry out the CLSM experiments.

2.1. Experimental characterization

For porosity, permeability and specific surface area determinations

four measurements were performed with a sample stack of each two 47 mm diameter membranes. Capillary Flow porometry experiments were carried out eight times on every 25 mm diameter sample.

2.1.1. Porosity determination (PD)

For porosity determination, four stacks of two 47 mm membrane samples were weight in a dried and in a completely wet (purified water) state. Membrane samples were dried in an oven at 80 $^{\circ}\text{C}$ until the weight reached a constant value indicating that all water from within the microstructure had evaporated. Afterwards the membranes were wetted with purified water and then weighed again. Assuming a full penetration of purified water in the accessible pore volume, the porosity ϕ was determined as

$$\phi = \frac{m_{\text{ROW}} - m_{\text{dry}}}{V_{\text{Membrane}} \cdot \rho_{\text{ROW}}} \quad (1)$$

where m_{ROW} is the mass of the fully wetted membrane, m_{dry} the mass of the dried membrane, ρ the density of water and V_{Membrane} the volume of the membrane sample.

2.1.2. Specific surface area (BET)

The BET-method determines the specific surface area S_{BET} on the basis of gas adsorption of nitrogen on the membrane sample, according to the following [5]

$$S_{\text{BET}} = \frac{N_{\text{A}} A_{\text{M}} V_{\text{Mono}}}{m_{\text{ges}} V_{\text{M}}} \quad (2)$$

where N_{A} is the Avogadro constant, A_{M} is the area of the adsorbed molecule, V_{Mono} is the volume of the adsorbed monolayer, m_{ges} the sample mass and V_{M} is the molar volume of adsorbed molecules. The membranes were heated for 24 h at 100 $^{\circ}\text{C}$ under vacuum. All measurements were performed on a Gemini V (micromeritics instrument Corp.).

2.1.3. Capillary flow porometry (CFP)

The membrane samples were wetted with Porefil[®] due to its qualities as a solvent with a low surface tension and vapor pressure (16 mN \cdot m⁻¹; 399 Pa) and its hydrophobic properties as a perfluoroether, which does not cause the membrane to swell. In the next step, nitrogen is perfused through the membrane in the pressure scan method [4] whereby the pores filled with the Porefil[®] will be completely depleted so that the membrane is liquid free. For the depletion, the pressure is increased continuously following a predefined pressure ramp. Subsequently, the measurement was repeated with the dry sample. For further analysis, the flow in relation to the nitrogen pressure is recorded [18]. Owing to the fact, that the pressure-difference between the measurements of the wet and the dry sample p is proportional to the pore size diameter d , a pore size distribution can be determined via the Young-Laplace-equation

$$\Delta p = \frac{4 \cdot \sigma \cdot \cos(\theta) \cdot a}{d} \quad (3)$$

σ is the surface tension, θ the wetting angle of the applied fluid, in this case it is assumed to be 0 $^{\circ}$, and a is the shape factor for the assumption of a certain 2D pore geometry. In this case a shape factor of 0.715 was used according to literature [19]. The point where the half dry curve, dividing all values for the flow in the dry-curve by two, and the wet curve meet defines the mean pore size. Due to the cumulative nature of this method, inhomogeneities in the pore structure are not detectable. This technique accounts for pores contributing to flow. For most applications, a consideration of these pores is sufficient as these often determine the performance or the selectivity of the membrane. However, a consideration of the entire pore structure and the homogeneity

of it is particularly useful for lateral flow membranes, since in these applications, pore inhomogeneities can have a significant influence on their performance. [20] All measurements were performed with the Porolux500 from Porometer.

2.1.4. Water permeability measurements (WPM)

The water permeability measurements were performed by using a permeability measurement device consisting of a cylindrical receptical (Stainless Steel Pressure Holder, 47 mm diameter membrane samples on a mesh grid, 200 mL capacity, Sartorius Stedim Biotech GmbH) in which a stack of two prewetted membranes were installed. Afterwards, the receptical was filled with 150 mL of purified water (pH 7.0) and a pressure of 50 mbar is applied while the hydrostatic pressure of the water column is considered. After opening a valve, the purified water is passing the membrane stack and the permeating water is weighed over time to calculate the permeability using Darcy's law (see Eq. (8)) [21].

2.2. Confocal laser scanning microscopic (CLSM) characterization

10 mm diameter membrane samples were used as described before. The CLSM experiments were performed in the center of each membrane cut-out. Prior to investigation the membrane sample has to be labeled with a fluorescence dye to ensure the visualization in the CLSM experiment.

2.2.1. Labeling of the nitrocellulose diagnostic membrane

For the fluorescent labeling of the nitrocellulose membrane, the 10 mm diameter samples were each gently shaken for 16 h in 1 mL of a solution containing 1 M HCl and 1 mol/L Cu(I)Cl in order to reduce the nitro groups into primary amines in a modification of the protocol by Owsley et al. [22]. After washing with purified water, the membrane samples were dried for 30 min at 80 °C in an oven. The dry samples were incubated in 1 mL of a solution of 32.5 mg. L⁻¹ Alexa Fluor 594 succinimidyl ester in 1 M KPI pH 7.0 and continuously stirred for 2 h. Finally, the labeled membrane samples were washed 3 times in purified water for 30 min to remove excess dye and were afterwards dried again for 1 h at 80 °C.

2.2.2. Microscope setup and experiment

The dry samples of labeled membrane were mounted on a microscope slide (Fisher Scientific GmbH, Ultra White Glass; 75 mm × 25 mm × 1 mm) and soaked in immersion oil (Leica Type F; refractive index of 1.512). Afterwards a cover slip (Fisher Scientific GmbH; 20 mm × 20 mm × 0.25 mm) was placed on the membrane sample and the edges were sealed with a two component adhesive. By placing the dried dyed membrane sample in immersion oil, the macroporous polymer membrane becomes transparent due to the refractive index matching [15]. This allows for the scanning laser to penetrate the whole depth of the membrane while the location of the surface-bound fluorescent labels retains the structural information. The fluorescence microscope TCS SP-8 confocal platform from Leica was used. For all measurements, a 63x oil-objective with a free working distance of 1.4 mm (HC PL APO 63x/1.40 Oil CS2 from Leica) and an DPSS laser (excitation wavelength: 561 nm) was employed.

The pinhole was set to 95.6 μm. The value for the smart gain was 650 V. Every sample was recorded with a resolution of 240.5 nm/voxel. The image size is 256 × 256 pixel which corresponds to an edge length of 61.56 μm for x- and y-direction, respectively. Overall, 590 images were taken in z-direction representing a depth of penetration of 141.89 μm. A total of 16 complete representations were recorded in the center of each membrane sample for the following analysis to enable an statistical evaluation and an experimental standard deviation.

2.2.3. Reconstruction of the sampled data

In order to employ the computer-assisted methods, image processing steps are applied to the obtained CLSM images. The image stack is filtered by a Median filter (2pixel) which reduces the noise of the images. Subsequently, the threshold is set to 0 and 170 respectively and a binarized stack of images results. The threshold values were adjusted such that resulting porosity of the binarized stack matches the one obtained by the experiment (Fig. 3). The binarized stack is finally assembled into the reconstructed 3D microstructure of the macroporous polymer membrane (see Fig. 2). For the image processing procedure, the software package ImageJ 1.51j8 was used [23].

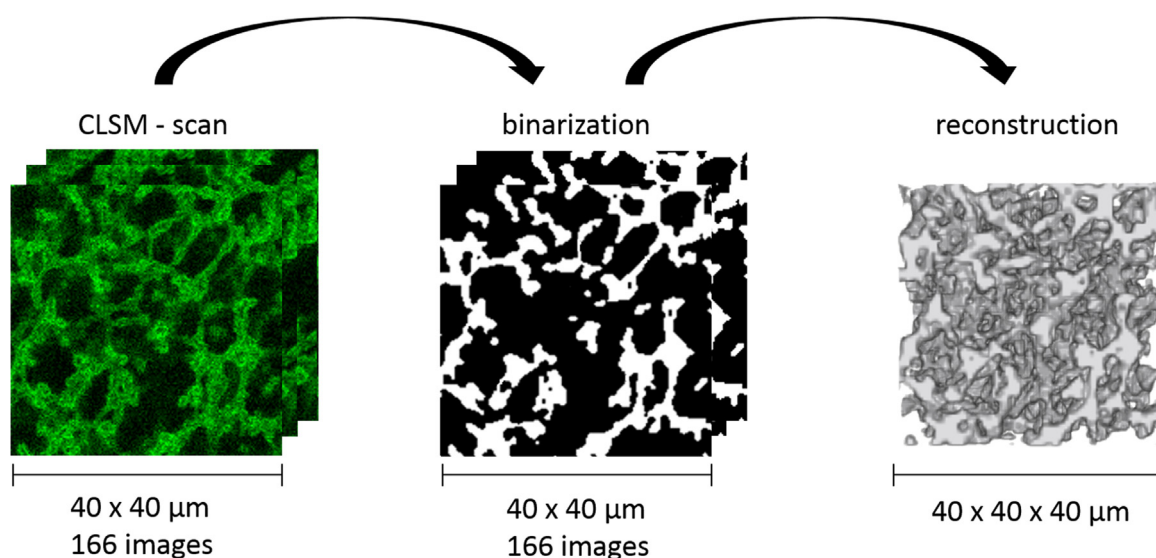


Fig. 2. Image processing procedure for the reconstruction of the porous membrane microstructure with the CLSM-scan (left), the filtered and binarized images (middle) and the resulting reconstructed 3D microstructure (right).

2.3. Computer-assisted characterization

The computer-assisted characterization incorporates numerical fluid flow simulations as well as post-processing steps. Both are conducted with tools and solvers which are implemented in the simulation framework *PAGE3D* [24]. For porosity and specific surface area determination, 16 representations were evaluated to calculate the experimental standard deviation. For permeability and pore size distribution determination, 5 representative 3D structures were evaluated as described in Sections 2.3.4, 2.3.5 and 2.4. In order to obtain the experimental standard deviation for these membrane characteristics, 5 different 3D structures were chosen from the results of the 16 determined porosities. To ensure an accurate standard deviation for these 5 chosen experiments, the 2 representations with the highest porosity, the 2 representations with the smallest and one representation with the mean porosity were chosen for the further determination of permeability and pore size distribution.

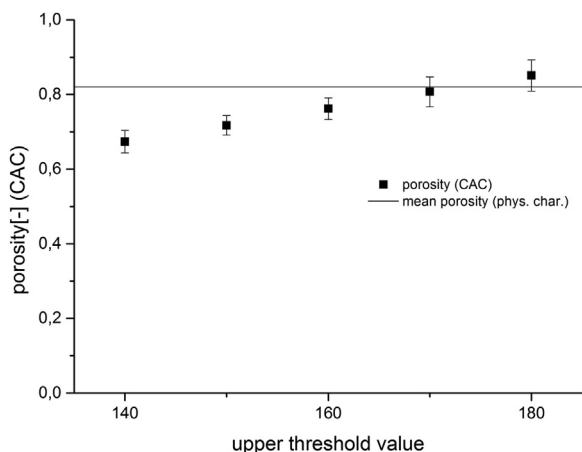


Fig. 3. Dependency of the CAC determined porosity to the set upper threshold value.

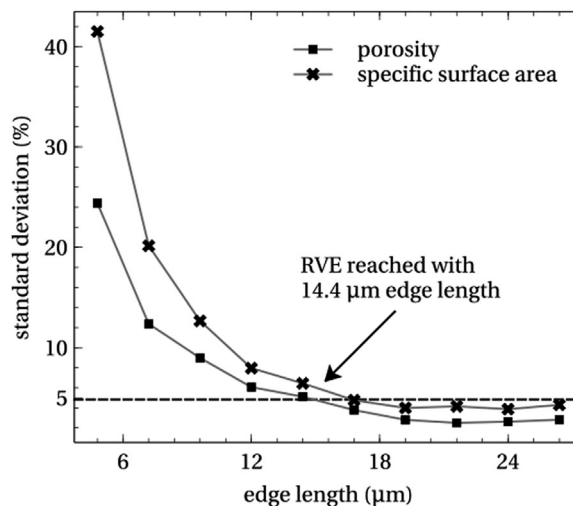
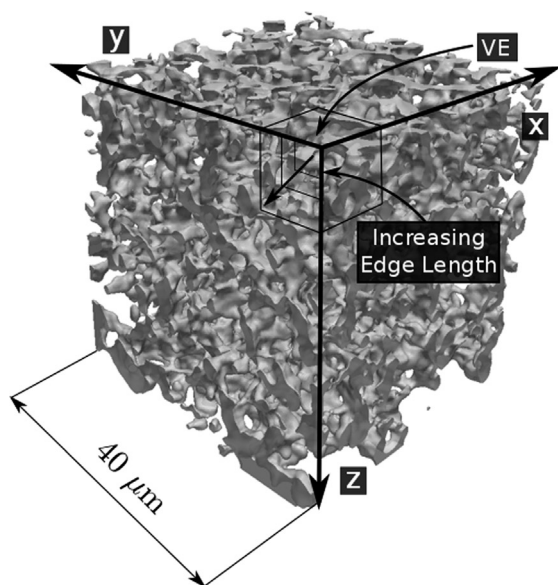


Fig. 4. Determination procedure for the representative volume element (RVE) with the reconstructed microstructure (left) and the resulting RVE size (right). The RVE is reached at 14.4 μm.

2.3.1. Porosity

The porosity ϕ is calculated from the ratio of the pore volume V_p to the total volume V_t as

$$\phi = \frac{V_p}{V_t} \tag{4}$$

Since the representation of pore and total volume is voxel-based, the porosity is determined by summing up the voxels of each volume.

2.3.2. Specific surface area

The specific surface area S_v is calculated as the ratio of the inner surface of the microstructure S_i to the total volume of the microstructure

$$S_v = \frac{S_i}{V_t} \tag{5}$$

The determination of the inner surface is based on blurring the boundaries between the structure and pore region by using a Gaussian filter and by calculating and summing up the surface normals in the diffuse interface.

2.3.3. Determination of the representative volume element

In order to reduce the influence of geometric heterogeneity of the microstructure for the characterization procedure it is necessary to determine a statistically representative volume element (RVE) which holds all the properties of interest. The RVE can be obtained by continuously increasing the edge length of an extracted volume element (VE) by means of increasing the number of voxels within the VE and estimating the porosity and specific surface as geometrical properties [25,26]. Therefore, the edge length is varied from 20 voxels up to 120 voxels per VE and in total, 50 different volume elements are distributed in the reconstructed microstructure while the spatial resolution is kept constant at 240 n m/pixel. When the standard deviation of the properties drops below 5 %, the size of the RVE is achieved. In Fig. 4 the determination procedure is schematically shown and depicted with the resulting RVE edge length of 14.4 μm. This leads to the conclusion that the used representations of 61.56 μm × 61.56 μm × 141.89 μm is representative in terms of a statistical evaluation.

2.3.4. Water permeability

The water permeability K of the membranes is calculated by solving the Stokes equations in the pore space of the microstructure numerically. With the assumption of dominating low flow velocities within the pores, the resulting advective inertial forces are small compared to the viscous forces which yields a low Reynolds number ($Re \ll 1$) for the flow problem. The advective force can then be neglected and the full Navier-Stokes equation can be linearized to the following Stokes equation

$$\mu \nabla^2 \mathbf{u} - \nabla p = 0 \quad (6)$$

with

$$\nabla \cdot \mathbf{u} = 0. \quad (7)$$

Herein, μ describes the dynamic viscosity of the fluid and \mathbf{u} is the velocity vector. For solving the set of linear partial differential equations, a pressure gradient in cross flow direction z (see Fig. 5) is defined as boundary condition while the inner surface of the microstructure is assumed to reveal no-slip boundary condition. For the remaining boundaries, slip condition is set. The velocity field, which adjusts at a given pressure gradient ∇p , is used for the permeability estimation by using Darcy's law [27]

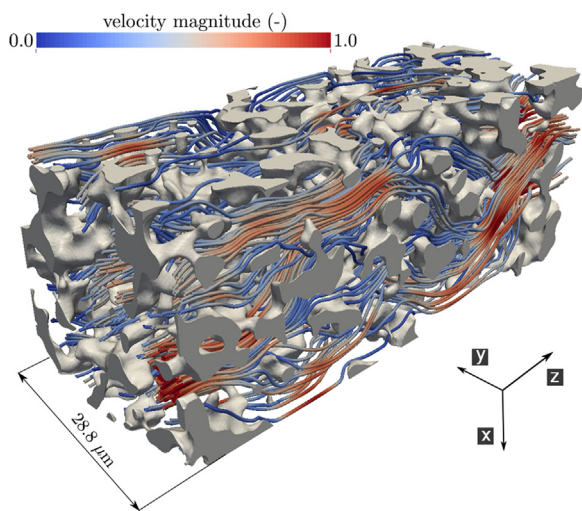


Fig. 5. Fluid flow simulation in crossflow direction (z -direction) on the pore-scale.

$$\mathbf{K} = \mathbf{u} \cdot \mu \cdot \frac{l}{\nabla p} \quad (8)$$

where l is the membrane thickness and \mathbf{K} describes the permeability tensor of the macroporous membrane.

2.3.5. Representative resolution for permeability determination

For the numerical fluid flow simulations it is important, besides a minimum physical edge length of the RVE, to apply a reasonable numerical resolution for the pore space in order to minimize discretization errors during the solving of Eq. (6) numerically. In contrast to the given spatial resolution of the images, the numerical resolution can be modified by increasing the number of voxels used to represent the computational grid for the pore space in the 3D microstructure. As a consequence, the modified voxel size changes as well. In order to determine the minimal voxel size needed, a 3D section $26.4 \mu\text{m} \times 26.4 \mu\text{m} \times 141.89 \mu\text{m}$ of the microstructure is extracted. Herein, the voxel size is decreased while the number of voxels increases. In order to guarantee the conservation of the morphology when the numerical resolution is changed, the binarized 3D data (see Fig. 2) is blurred by a Gaussian filter first. Then, the grid refinement is obtained by increasing the domain size by 2, 4 and 5 times followed for each time by a tri-linear

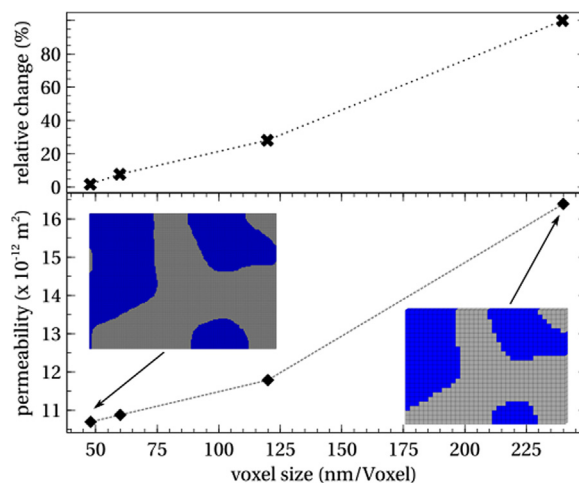


Fig. 6. Determination of the minimum voxel size (spatial resolution) of the investigated microstructure.

interpolation of the original blurred values on the refined grid. As a final step, the refined domain is binarized again. Starting with a voxel size of 240 nm the permeability is calculated for each numerical resolution. By assuming to have a maximum relative deviation with the lowest numerical resolution, the relative error for the permeability values is decreasing with an increasing numerical resolution. For an increased voxel size from 60 nm to 48 nm the achieved relative error is 1.67% which marks the minimum numerical resolution needed. The determination of the permeability values and the corresponding relative deviations are illustrated in Fig. 6. In order to minimize the discretization error for the permeability estimations, a discrete mesh with about 221.000.000 calculation points is needed. For the numerical simulations 193 CPU's of the ForHLR II supercomputer in Karlsruhe are used in parallel.

2.4. Pore size distribution

An image processing method was developed to determine the pore size distribution on the micro-scale. This method can be divided into three processing steps:

- i) Solving a signed distance function (SDF)
- ii) Determination of the medial axis (MA)
- iii) Filtering the solution of the signed distance function by the medial axis

2.4.1. Signed distance function (SDF)

With the signed distance function $f(\mathbf{x})$ the shortest Euclidean distance to the nearest point in the boundary $\partial_s \Omega$ of a domain Ω is calculated based on the binary representation of the microstructure $g(\mathbf{x})$ [28,29]. Once the SDF is initialized by $f(\mathbf{x}) = g(\mathbf{x})$, the distance of each point to the boundary can be calculated by setting the magnitude of the gradient of the normal vector relative to the boundary to be unity as

$$|\nabla f(\mathbf{x})| = 1 \quad (9)$$

The solution of this condition is determined iteratively by solving a partial differential equation (PDE) in 3D space.

$$\frac{\partial f(\mathbf{x})}{\partial t} = S(f) \cdot \text{sign}(f) \cdot (1 - |\nabla f|) \quad (10)$$

Herein, the function sign is responsible for distinguishing between the two sides of the boundary region $\partial_s \Omega$

$$\text{sign}(f) = \begin{cases} 1 & \text{if } f(\mathbf{x}) \in \Omega^+ \\ -1 & \text{if } f(\mathbf{x}) \in \Omega^- \\ 0 & \text{if } f(\mathbf{x}) \in \partial_s \Omega \end{cases}$$

where the domain is divided into inside (Ω^+) and outside (Ω^-) the region of interest (pore space). In order to fix the boundaries for the SDF solution, the smearing function $S(f)$ is used

$$S(f) = \frac{f}{\sqrt{f^2 + (\Delta x)^2}} \tag{11}$$

The PDE is solved with Godunov's upwind difference scheme [30].

2.4.2. Medial axis (Skeleton)

The medial axis (MA) is defined as the locus of all the centers of maximal spheres (green points in Fig. 7 (c)) which can be put into the geometry where the spheres touch the boundary at more than one point (red points in Fig. 7 (c)). The extraction of this medial axis can be approached by calculating the Hessian matrix of the signed distance field f and by identifying the local maxima of $f(\mathbf{x})$. However, this results in a point cloud which

represents an area around the medial axis but not a simple bounding line [31]. Another way of medial axis extraction is the application of thinning algorithms which lead to simple lines satisfying topological properties, but which do not deliver information about distances. In order to fulfill the ultimate aim of preserving the topology of the microstructure and to simultaneously represent it in a parametric manner, the signed distance function is combined with the medial axis obtained by a thinning algorithm.

The applied algorithm for the thinning procedure is based on Lee's algorithm [32] where by symmetrically eroding the geometry's surface, the topology is projected on the resulting thin line [33].

2.4.3. Combination of SDF and MA

The combination of both methods, namely the signed distance function and the medial axis extraction by the thinning algorithm, leads to the pore size distribution of the microstructure. It is realized by first solving the PDE for the distance field and then filtering the distance field by the points which belong to the obtained medial axis. The filtered distances are then interpreted as radii of different pores where the information about the pore position is delivered by the medial axis.

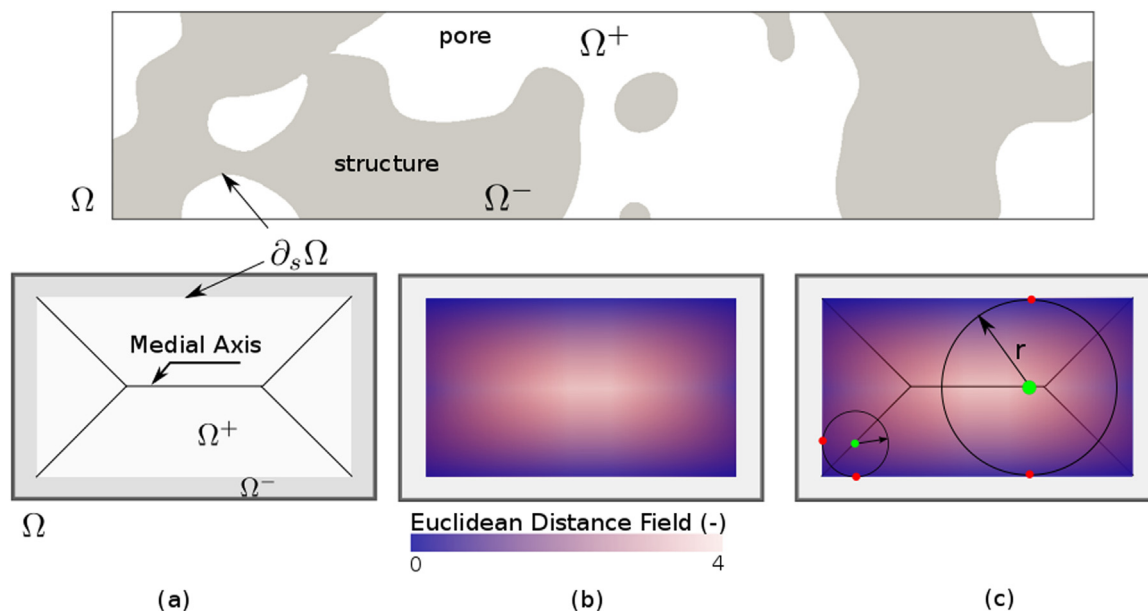


Fig. 7. Schematic description of the processes for the computer-assisted determination of the pore size distribution in a domain Ω with the structure surface $\partial_s \Omega$. (a) Determination of the Medial Axis (MA); (b) Solving the signed distance function (SDF); (c) Filtering the SDF by the MA.

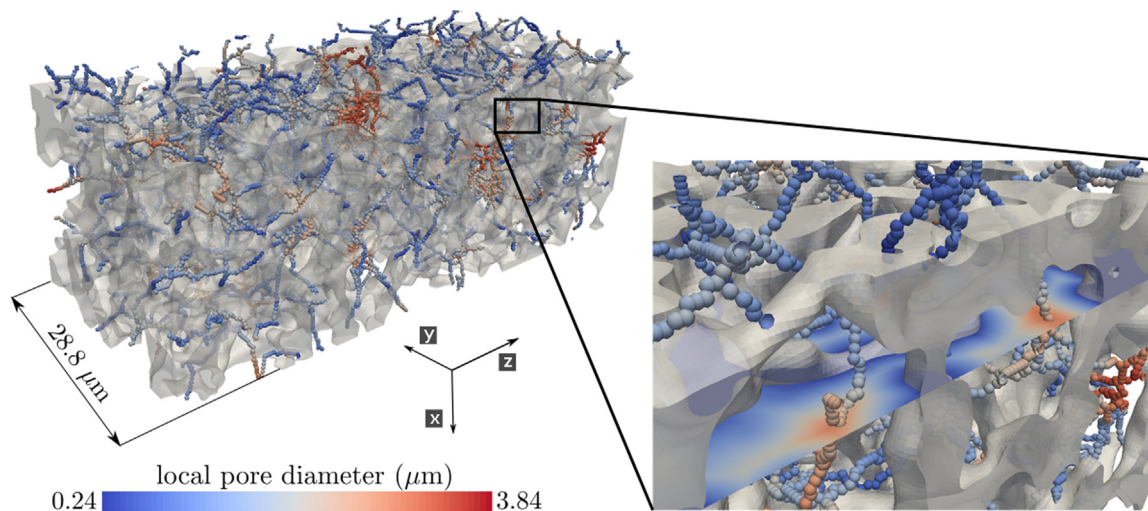


Fig. 8. Illustration of the geometrical porometry by using the signed distance field and the extracted medial axis in a section of the reconstructed CLSM-scans.

With this method, the pore space is approached by many differently sized spheres while neighboring spheres are allowed to overlap. Furthermore, local information about the pore sizes are accessible as well as the overall information about pore size distribution and the resulting mean pore size can be derived. Fig. 7 illustrates the whole procedure by simplifying the pore space of the complex microstructure to a simple 2D rectangle while Fig. 8 shows this in the complex 3D structure. In the latter, the pathway of the medial axis is visualized by beads which are color coded by the corresponding local diameter of the pores.

3. Results and discussion

The presented results for CAC measurements were performed with 3D representations of $61.56 \mu\text{m} \times 61.56 \mu\text{m} \times 141.89 \mu\text{m}$ (Section 2). These 3D structures are representative with respect to the obtained RVE with a minimum voxel edge length size of $14.4 \mu\text{m}$ (Section 2.3.3). However, the shown exemplary Figs. 9 and 10 refer to the same 3D representation.

3.1. Porosity, specific surface area and permeability measurements

The physical characterization of the porosity and the specific surface area were performed by weighing the dry and water wetted

membrane and measuring the BET nitrogen adsorption, respectively. In contrast to those methods the here presented CAC provides the opportunity to calculate the membrane characteristics in total or locally on the pore-scale and with respect to every axis of the membrane (Fig. 9).

The CAC derived total porosity of the membrane is, as expected, in good agreement to the experimental measurements as shown in Table 1 due to the way we chose to set the threshold (Section 2.2.3). The local determination over the z axis shows that the membrane consists of a homogeneous porosity over the z-axis. The observed increase at the upper respectively the lower edge of the membrane is probably caused by the roughness of the membrane surface (Fig. 1, 9). In addition, the onset on the edge of the membrane is often not flat so that the porosity determination is challenging in this section of the membrane. The local determination of the specific surface area by CAC shows an increase at the edges fitting the therein detected higher porosity (Fig. 9).

Overall the specific surface area is quite homogeneous matching the homogeneous porosity over z-axis. Nevertheless it clearly can be seen, that the investigated macroporous membrane shows no significant gradient in terms of porosity and specific surface area over the thickness of the membrane, a fact which cannot be detected by physical porosity determination or BET analysis (Fig. 9). The absolute value for the specific surface area determined by CAC is however

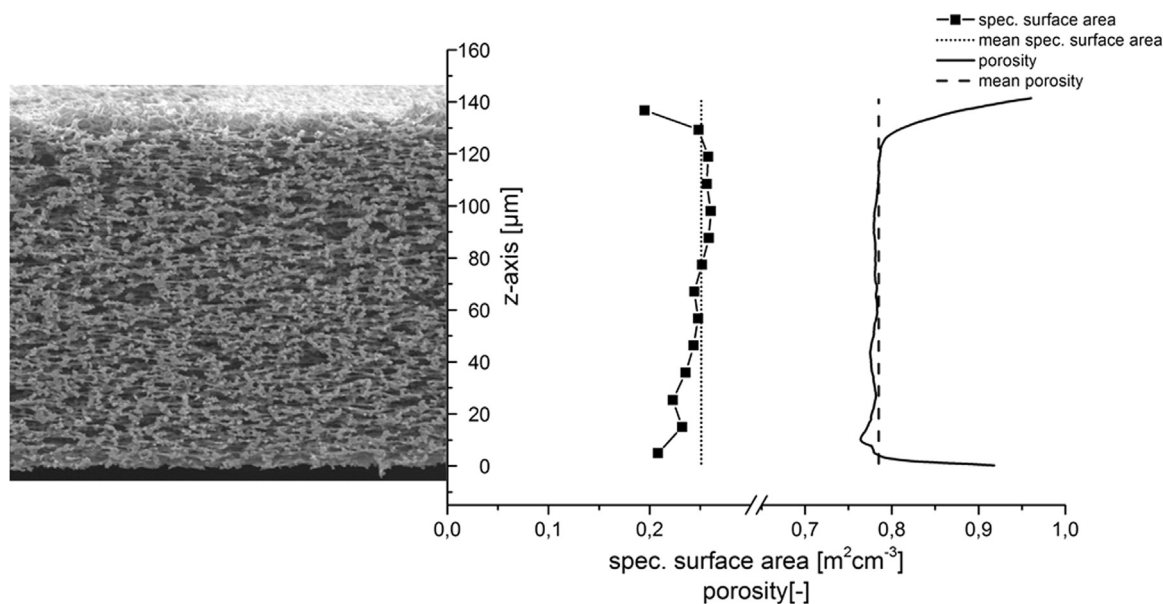


Fig. 9. Porosity and specific surface area along the z-axis in comparison with a SEM cross section (scaling: $155 \mu\text{m}$ height \times $165 \mu\text{m}$ length).

Table 1

Physical and CAC determined characteristics for porosity, the specific surface area, the water permeability and the mean pore size for the macro porous nitrocellulose membrane.

Property	PD	BET	WPM	CFP	CAC
Porosity (-)	0.82 ± 0.02	-	-	-	0.79 ± 0.02
Specific surface ($\text{m}^2 \cdot \text{mL}^{-1}$)	-	0.69 ± 0.09	-	-	0.27 ± 0.02
Water permeability ($\times 10^{-13} \text{m}^2$)	-	-	9.92 ± 0.96	-	9.41 ± 1.22
Mean pore size (μm)	-	-	-	3.05 ± 0.09	3.74 ± 0.19

significantly smaller than in the nitrogen adsorption experiments (Table 1). An explanation is that the resolution of the images by CLSM is not high enough to represent the surface roughness on a molecular level as in the nitrogen adsorption experiments. The surface roughness does not have a significant impact on porosity, water permeability and pore size distribution by CAC determinations but in terms of the specific surface area it leads to a smaller determined surface area in CAC in comparison to the BET analysis.

The water permeability simulations were performed with a resolution of 48 nm voxel edge length like described in Section 2.3.5. Due to the fact that the water permeability simulation experiments need sufficient information in z-direction, no local determination was considered. However the overall water permeability out of CAC, given in Table 1, is in very good agreement with the experimentally determined values. The quantified water permeability additionally confirms the 3D morphology as well as the determined structure characteristics.

3.2. Computer-assisted determination of the pore size distribution

The pore size distribution was determined on the same representations used for the water permeability simulations as districted in Section 2.4 (Fig. 8). In Fig. 10 the cumulative and the relative pore size distribution are displayed. A normal distribution fits the data for the relative pore size distribution reasonably well. This indicates, that the pore sizes are symmetrically distributed around the mean pore size determined to be 3.59 μm in this example. The comparison of the fitted distribution out of CAC and the experimental pore size distribution out of capillary flow porometry illustrates that the experimentally observed mean pore size of the membrane is smaller than the CAC data (Table 1). The experimental results further exhibit a small distribution of pore sizes compared to the CAC analysis.

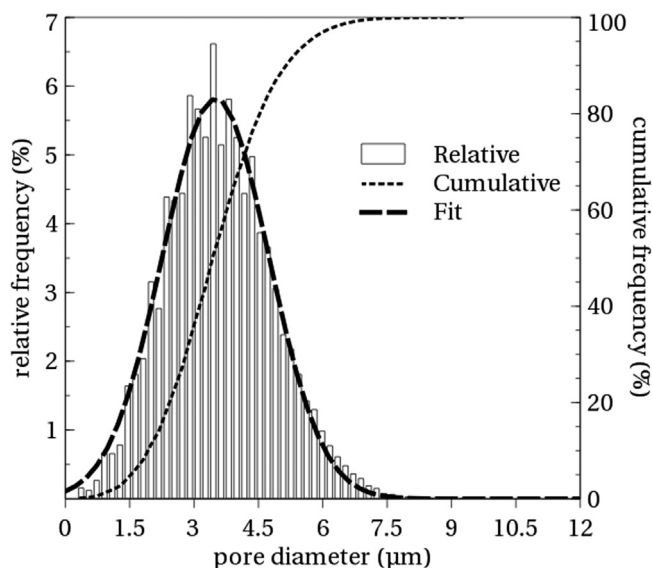


Fig. 10. Geometrical pore size distribution for both, relative and cumulative frequency, obtained by the presented image analyzing method. The mean pore size of this representation of the diagnostic membrane is determined as 3.59 μm .

4. Conclusion

The presented computer assisted characterization (CAC) method was successfully used to characterize a macroporous nitrocellulose diagnostic membrane. Typical membrane structure characteristics like the porosity, the specific surface area, and the pore size distribution were determined in reasonable agreement with the experimental results obtained by standard membrane characterization techniques. In addition the permeability was simulated with a Stokes approach to further evaluate the structure characteristics by CAC. These results are in good accordance with experimental measurements. The presented methods are capable to reproduce results with common techniques and moreover enable to quantify gradual changes of the porosity and the membrane structure with a local parameter analysis along the z-axis (Fig. 9). The new combined experimental and computational techniques facilitate a quantitative evaluation of the heterogeneities of a macroporous membrane structure. Additionally the characteristic microstructure parameters were determined by CLSM experiments in comparison to three different experimental measurements. In further investigations CAC can be employed to specify a particular membrane type for the use in capillary flow porometry to incorporate a 3D geometrical pore structure information instead of the nowadays commonplace 2D shape information [4,19].

Acknowledgment

This work was supported by Sartorius Stedim Biotech GmbH in Goettingen, Germany. Herein we thank Sinja Pagel for fundamental measurements on the CAC and also Marcel Bremerich, Florian Taft and Louis Villain for the rich discussions. We acknowledge the Max-Planck-Institute for Biophysical Chemistry. A special thanks herein to Dirk Kamin from the working group of Stefan Hell for the opportunity to measure CLSM and the given support. We further acknowledge the financial support from the German government through the BMBF project OptiProt. Furthermore, the fluid flow simulations were performed on the computational resource ForHLR II funded by the Ministry of Science, Research and the Arts Baden-Württemberg and the DFG (“Deutsche Forschungsgemeinschaft”).

References

- [1] T. Young, An essay on the cohesion of fluids, *Philos. Trans. R. Soc. Lond.* 95 (1805) 65–87.
- [2] P.S. Laplace, *Traité de mécanique céleste/par PS Laplace...; tome premier* [-quatrième], De. l’Impr. De. Crapelet 4 (1805).
- [3] C. Agarwal, A.K. Pandey, S. Das, M.K. Sharma, D. Pattyn, P. Ares, A. Goswami, Neck-size distributions of through-pores in polymer membranes, *J. Membr. Sci.* 415 (2012) 608–615.
- [4] M. Halisch, E. Vogt, C. Müller, D. Pattyn, P. Hellebaut, K. Van Der Kamp, Capillary flow porometry - assessment of an alternative method for the determination of flow relevant parameters of porous rocks, in: *Proceedings of the Annual Symposium of the Society of Core Analysts, Napa Valley, USA (2013)* ResearchGate.
- [5] S. Brunauer, P. Emmett, E. Teller, Adsorption of gases in multimolecular layers, *J. Am. Chem. Soc.* 60 (2) (1938) 309–319.
- [6] A. Hernández, J. Calvo, P. Prádanos, F. Tejerina, Pore size distributions in microporous membranes. a critical analysis of the bubble point extended method, *J. Membr. Sci.* 112 (1) (1996) 1–12.
- [7] G. Reichelt, Bubble point measurements on large areas of microporous membranes, *J. Membr. Sci.* 60 (2) (1991) 253–259.
- [8] S. Wickramasinghe, J. Carlson, C. Teske, J. Hubbuch, M. Ulbricht, Characterizing solute binding to macroporous ion exchange membrane adsorbers using confocal laser scanning microscopy, *J. Membr. Sci.* 281 (1) (2006) 609–618.
- [9] M. Marroquin, T. Bruce, J. Pellegrino, S.R. Wickramasinghe, S.M. Husson, Characterization of asymmetry in microporous membranes by cross-sectional confocal laser scanning microscopy, *J. Membr. Sci.* 379 (1) (2011) 504–515.

- [10] S. Barbe, E. Boller, R. Fáber, V. Thom, T. Scheper, The use of x-ray microtomography for the characterization of macroporous membranes, at Journée annuelle de la Société Française de Métallurgie et de Matériaux, Saint Etienne (France) (2007) S. Barbe.
- [11] R. Ziel, A. Haus, A. Tulke, Quantification of the pore size distribution (porosity profiles) in microfiltration membranes by sem, tem and computer image analysis, *J. Membr. Sci.* 323 (2) (2008) 241–246.
- [12] H. Reingruber, A. Zankel, C. Mayrhofer, P. Poelt, Quantitative characterization of microfiltration membranes by 3d reconstruction, *J. Membr. Sci.* 372 (1) (2011) 66–74.
- [13] H. Reingruber, A. Zankel, C. Mayrhofer, P. Poelt, A new in situ method for the characterization of membranes in a wet state in the environmental scanning electron microscope, *J. Membr. Sci.* 399–400 (2012) 86–94.
- [14] C. Charcosset, J.-C. Bernengo, Comparison of microporous membrane morphologies using confocal scanning laser microscopy, *J. Membr. Sci.* 168 (1) (2000) 53–62.
- [15] C. Charcosset, A. Cherfi, J.-C. Bernengo, Characterization of microporous membrane morphology using confocal scanning laser microscopy, *Chem. Eng. Sci.* 55 (22) (2000) 5351–5358.
- [16] G.E. Fridley, C.A. Holstein, S.B. Oza, P. Yager, The evolution of nitrocellulose as a material for bioassays, *MRS Bull.* 38 (4) (2013) 326–330.
- [17] D. Wild, *The immunoassay handbook: theory and applications of ligand binding, ELISA and related techniques*, Newnes, 2013.
- [18] M. De Bruyne, R. De Bruyne, R. De Moor, Capillary flow porometry as assess the seal provided by root-end filling materials in a standardized and reproducible way, *J. Am. Chem. Soc.* 60 (2) (1938) 309–319.
- [19] J. Akshaya, K. Gupta, Liquid extrusion techniques for pore structure evaluation of nonwovens, *Int. Nonwovens J.* 12 (3) (2003) 45–53.
- [20] A.L. Ahmad, S.C. Low, S. Shukor, A. Ismail, Synthesis and characterization of polymeric nitrocellulose membranes: influence of additives and pore formers on the membrane morphology, *J. Appl. Polym. Sci.* 108 (4) (2008) 2550–2557.
- [21] J. Schwellenbach, P. Kosiol, B. Sölter, F. Taft, L. Villain, J. Strube, Controlling the polymer-nanolayer architecture on anion-exchange membrane adsorbers via surface-initiated atom transfer radical polymerization, *React. Funct. Polym.* 106 (2016) 32–42.
- [22] D. Owsley, J.J. Bloomfield, The reduction of nitroarenes with iron/acetic acid, *Synthesis* 2 (1977) 118–120.
- [23] C.A. Schneider, W.S. Rasband, K.W. Eliceiri, Nih image to imagej: 25 years of image analysis, *Nat. Methods* 9 (7) (2012) 671–675.
- [24] J. Hötzer, A. Reiter, H. Hierl, P. Steinmetz, M. Selzer, B. Nestler, The parallel multi-physics phase-field framework pace3d, *J. Comput. Sci.* (2018).
- [25] E. Brun, J. Vicente, F. Topin, R. Occelli, M.J. Clifton, Microstructure and transport properties of cellular materials: representative volume element, *Adv. Eng. Mater.* 11 (10) (2009) 805–810.
- [26] X. Huang, Q. Wang, W. Zhou, D. Deng, Y. Zhao, D. Wen, J. Li, Morphology and transport properties of fibrous porous media, *Powder Technol.* 283 (2015) 618–626.
- [27] M. Röding, E. Schuster, K. Logg, M. Lundman, P. Bergström, C. Hanson, T. Gebäck, N. Lorén, Computational high-throughput screening of fluid permeability in heterogeneous fiber materials, *Soft Matter* 12 (29) (2016) 6293–6299.
- [28] M. Sussman, P. Smereka, S. Osher, A level set approach for computing solutions to incompressible two-phase flow, *J. Comput. Phys.* 114 (1) (1994) 146–159.
- [29] G. Russo, P. Smereka, A remark on computing distance functions, *J. Comput. Phys.* 163 (1) (2000) 51–67.
- [30] O. Nilsson, A. Söderström, Euclidian distance transform algorithms: A comparative study (2007).
- [31] H. Xia, P.G. Tucker, Distance solutions for medial axis transform, in: *Proceedings of the 18th International Meshing Roundtable* (2009) 247–265.
- [32] T.-C. Lee, R.L. Kashyap, C.-N. Chu, Building skeleton models via 3-d medial surface axis thinning algorithms, *CVGIP: Graph. Models Image Process.* 56 (6) (1994) 462–478.
- [33] H. Homann, Implementation of a 3d thinning algorithm, *Insight J.* 421 (2007).